Quantum dot microcavity control of photon statistics

Snijders, H.J.

Chapter 7

Fiber-coupled cavity QED source of identical single photons

We present a fully fiber-coupled source of high-fidelity single photons. This is achieved by embedding an InGaAs semiconductor QD in an optical Fabry-Perot microcavity with robust design and rigidly attached single-mode fibers which enables through-fiber cross polarized resonant laser excitation and photon extraction. Even without spectral filtering, we observe that the incident coherent light pulses are transformed into a stream of single photons with high purity (97%) and indistinguishability (90%), which is measured at an in-fiber brightness of 5% with an excellent cavity mode to fiber coupling efficiency of 85%. Our results pave the way for fully fiber integrated photonic quantum networks, further, our method is equally applicable for fiber-coupled solid-state cavity-QED based photonic quantum gates.

This Chapter has been published in Physics Review Applied 9, 031002 (2018) [4].

7.1 Introduction

Every isolated two-level quantum system such as an atom, ion, color center or QD, can in principle be turned into a bright single-photon source [104, 9]. Ideally, such a source produces a stream of single photons, never more or less than one photon per time bin, and all having the same Fourier limited spectrum and timing. Such a source would be essential for exploration of numerous quantum technologies such as optical quantum computing [105, 106, 107, 108] and simulation [109]. Further, the reduced fluctuations of such single-photon light would enable exciting opportunities everywhere where noise is a limiting factor, in fields from metrology to microscopy.

However, only very recently, high-fidelity single-photon sources have been demonstrated [2, 3, 110, 111, 112, 113] that simultaneously fulfill the key requirements: near-unity single-photon purity and indistinguishability of consecutively emitted photons, and a high brightness. For a single-photon source, high brightness and on-demand availability is crucial for efficient implementation of quantum photonic protocols. Additionally, to exploit the power of quantum interference, consecutively produced photons need to be indistinguishable, meaning that their wave functions must overlap well. Until recently, heralded spontaneous parametric down-conversion sources [114] were the state of the art for single-photon sources (SPS) [115], with which most quantum communication and optical quantum computing protocols have been demonstrated [116]. The main problem of these sources is that the Poissonian statistics of the generated twin photons will always result in a trade-off between single-photon purity (the absence of N>1 photon-number states) and brightness (the probability to obtain a photon per time slot).

One way to deterministically produce single photons is to use trapped atoms [117], where single-photon rates up to around 100 kHz have been obtained recently [118]. In order to enable integration and increasing the photon rate, solid-state systems have been investigated, in particular promising are semiconductor QDs [119, 9, 120]. QDs have nanosecond-lifetime transitions that enable GHz rate production of single photons as required for numerous quantum technologies. Compared to other solid-state emitters such as NV centers, nanowire QDs, excitons in carbon nanotubes or two-dimensional materials [121, 122], self-assembled QDs in cavities can show almost perfect purity and indistinguishability [2]. A challenging task is to couple the quantum emitter to propagating optical modes with near-unity efficiency. This can be achieved by placing them in optical micro cavities, which additionally increases the emission rate by cavity-QED Purcell enhancement, such as micropillar cavities [5, 9], photonic crystal cavities [66], or ring resonators [123].

For the next major step in implementing QD single-photon sources in complex photonic quantum networks, coupling to a single-mode optical fiber is essential. Several challenges are connected to this: cryogenic compatibility [124], resonant optical pumping, high coupling efficiency and robust and stable polarization control. Only recently, a first study on a non-resonantly pumped multi-mode fiber-coupled device appeared [125]. Another approach is to employ fiber-tip micro cavities but the photon collection efficiency is limited to about 10% to date [126, 127].

Here, we show a prototype of a fully fiber-coupled solid-state resonantly pumped and transmission-based source of identical photons.

7.2 Device structure & fiber coupling

Our fiber-coupled single-photon device is sketched in Fig. 7.1: The device consists of a layer of self-assembled InAs/GaAs QDs embedded in a micropillar Fabry–Perot cavity (maximum Purcell factor $F_p = 11.2$) grown by molecular beam epitaxy [73]. The QD layer is embedded in a P–I–N junction, separated by a 27 nm thick tunnel barrier from the electron reservoir to enable tuning of the QD resonance frequency by the quantum-confined Stark effect. Since we do not use air-guided micropillars but an oxide aperture for 3D confinement [128, 74], the device is very robust and the optical or QD properties do not degrade by attachment of the fibers. It also allows for precise alignment of the fibers, and therefore the use of single-mode fibers. This is essential not only for integration in larger quantum networks, but also to enable high-fidelity polarization control as we show here.

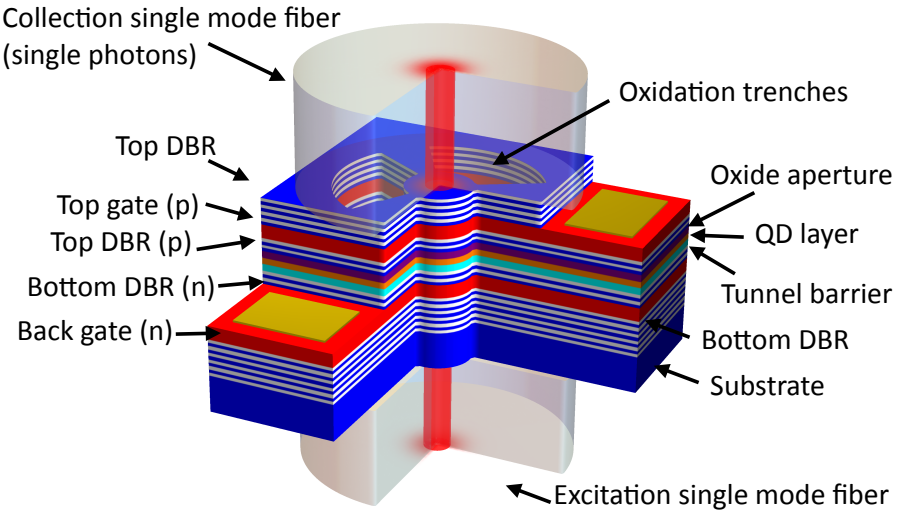

Figure 7.1: Sketch of the microcavity QD device with attached fibers from bottom (excitation fiber) and top (single photon collection fiber). The trenches are used for wet-chemical oxidation of a sacrificial AlAs layer to form an intracavity lens or aperture that leads to transverse confinement of the optical cavity mode.

Fig. 7.2 shows a microscope image of the fiber-coupled cavity-QED device, visible is the collections fiber attached to the sample and the bond wires connected to the gold bond pads. Single-mode fibers are attached to the front and back of the sample using a UV-curable Norland optical adhesive 81. Attaching the fibers to the device requires three steps (see Fig. 7.3). **Step 1:** The sample is mounted in an optical spectroscopy setup containing a long working distance microscope. The setup allows for precisely aligning the single-mode fibers with a motorized translation stage. **Step 2:** The collection fiber is aligned to the cavity mode by making use of an inverted microscope. The sample is imaged by sending through the fiber light from a Superlum 471-HP2 superluminescent diode with a broad (900-980 nm) spectrum. The micropillar trenches are observed with a CCD camera allowing for coarse alignment of the fiber to the center of the micropillar. Fine alignment is done by bringing the fiber closer to the sample and detecting the

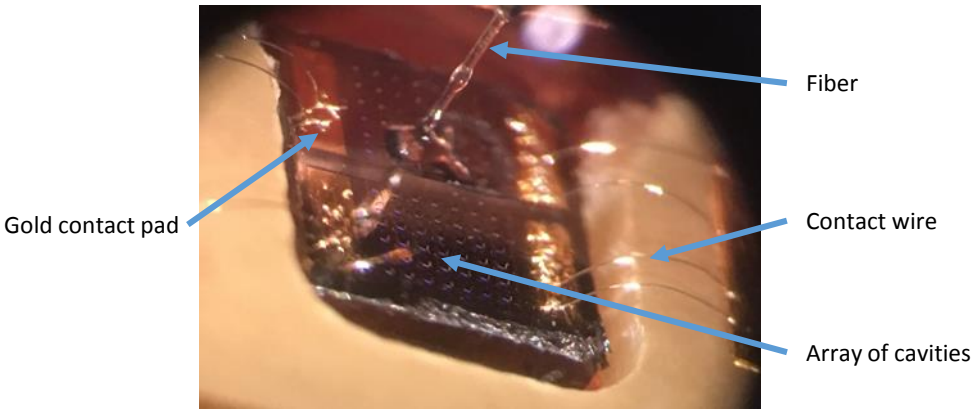

Figure 7.2: Microscope image of the fiber-coupled cavity-QED device.

resonantly transmitted light with a 1 m grating spectrometer. The optimal position is found by maximizing the fundamental mode of the cavity and reducing the transmission of the higher order TE/TM modes. Once the optimal position is found the single-mode fiber is moved up vertically so that a drop of Norland Optical Adhesive 81 can be put onto the cleaved fiber facet. After bringing the fiber back to its original position, the adhesive should touch the sample which is verified with an optical microscope. Again the position is optimized before the adhesive is cured using UV-light. Before removing the device from the setup, the fiber is firmly attached to the copper mount using Stycast for extra stability. **Step 3:** Excitation fiber attachment. We flip the device around and send broadband light into the collection fiber. Rough alignment of the excitation fiber at the bottom of the device is done by aligning the fiber to the fundamental cavity mode using the microscope, after which we use again a spectrometer to fine tune the position. Then, the procedure from step 2 is used for attaching the fiber.

The cavity mode of our device has at the front surface a waist of $\omega_{front} = 2.14 \pm 0.08\,\mu\text{m}$ and at the back a waist of $\omega_{back} = 28.48 \pm 1.02\,\mu\text{m}$ at around 955 nm [128]. The increased waist at the back of the sample is due to the 650 µm thick GaAs wafer. The fibers (Thorlabs 780HP) have a core radius of 2.2 µm and 0.13 NA, which results in a mode waist of $\omega_{fiber} = 2.95 \pm 0.25\,\mu\text{m}$. Neglecting the phase and only taking into account the mode waist of the fiber, we have at the front side of the cavity a coupling efficiency of [129]

$$\eta = \left(\frac{2\omega_{fiber}\,\omega_{front}}{\omega_{fiber}^2 + \omega_{front}^2} \right)^2 \exp\left(-\frac{2u^2}{\omega_{fiber}^2 + \omega_{front}^2} \right). \tag{7.1}$$

Here, u is the transverse misalignment. Setting $u = 0$ we obtain an optimal efficiency of $\eta_{front} = 90\% \pm 7.6\%$. Experimentally, we obtain for our device a coupling efficiency that is very close to this value ($85 \pm 11\%$, see section 7.9.3), confirming the high performance of the fiber attachment method. The fiber at the back of the sample has a reduced incoupling

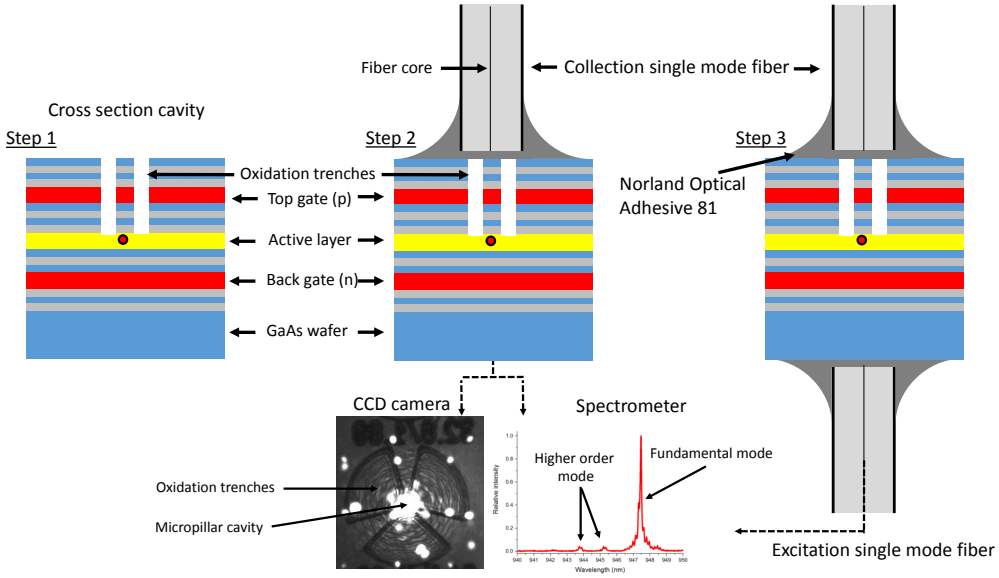

Figure 7.3: Sketch of the procedure for connecting single-mode fibers to the cavity-QED device.

efficiency of 0.6% due to the thick GaAs substrate. For operation of our single-photon source this reduced coupling efficiency is irrelevant because we excite the system from the back where the coupling efficiency only affects the required excitation laser power.

7.3 Optical setup

The optical setup used to measure photon correlations to obtain the single-photon purity and indistinguishability is shown in Fig. 7.4. A pulse delay setup can be used to create from a mode-locked 80 MHz Ti:Sa laser double pulses, which are sent to the micropillar cavity. The transmitted photons are analyzed with a Hanbury Brown Twiss setup to determine the second-order correlation function $g^{(2)}(\Delta\tau)$, or with a Mach-Zehnder interferometer to observe Hong-Ou-Mandel type photon bunching of consecutively emitted photons to determine their indistinguishability M. Almost all components in the setup are fiber-based or fiber-coupled, except the production of the double laser pulses and the polarizers (fiber U-benches). The delay between the double pulses is precisely adjusted to the Mach-Zehnder interferometer delay by scanning Δx while observing first-order interference in absence of the cavity-QED device. This interference signal becomes maximal when the position of Δx matches the in-fiber delay of about 5.2 ns.

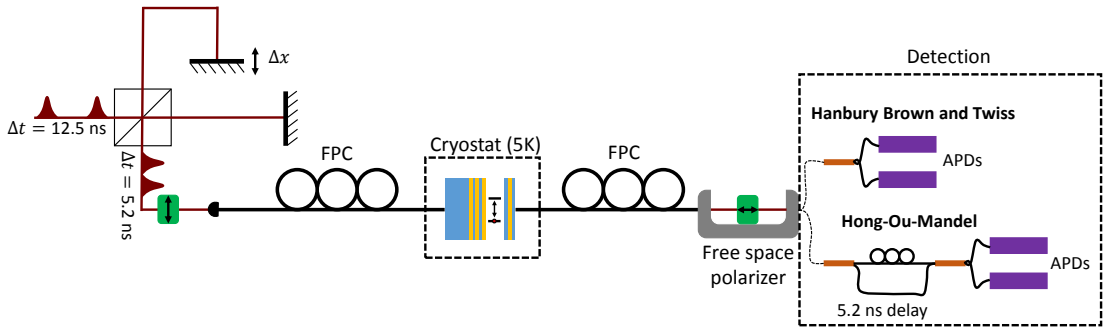

Figure 7.4: Sketch of the experimental setup. Dark red lines indicate free space laser light at around 932.58 nm, single-mode fibers are depicted in black. FPC: fiber polarization controller.

7.4 Transmission measurements

Now, we discuss the optical properties of the device, in all experiments presented here we investigate resonance fluorescence at a temperature of 5 K. The fundamental cavity mode is split in two linearly polarized modes, the H and V mode, induced by a small ellipticity of the cavity cross-section and material birefringence. Similarly, the neutral exciton transition of the QD is split in two linearly polarized transitions by the fine-structure exchange interaction. Fig. 7.5(a) shows a false color plot of the transmission as a function of the applied bias voltage and laser frequency. Using a free-space polarizer and a fiber polarization controller, the input polarization is set along the H cavity polarization axes. The transmitted light is sent to a single-photon detector. The two fine-structure split QD transitions are clearly visible as dips in the transmission spectrum that shift as a function of the applied electric field. A cross sectional plot of Fig. 7.5(a) (grey line) is shown in Fig. 7.5(c) (red line). The depth of the dips indicate that the "X" QD transition couples more efficiently to the H cavity mode than the "Y" QD transition. This is confirmed by comparison to a numerical model[37, 38] taking all relevant cavity-QED and polarization effects into account (section 7.9.1). From this model we also determine the angle θ between the X QD axis and the H cavity mode axis to be $\theta = 17°$, and the polarization splitting of the fundamental cavity mode (18 GHz).

Fig. 7.5(b, c) (blue line) show single photons that are filtered from the transmitted light with a combination of a fiber polarization controller and a free-space optical polarizer set to extinguish the transmitted laser light (cross polarization). We excite the system along the H cavity mode polarization but detect only photons emitted from the V-polarized cavity mode. This is ideal for efficient collection of the single photons that are coherently scattered from the Y-transition of the QD, as is seen in Fig. 7.5(b). This is a workable scheme because for excitation of the QD-cavity system, we can simply remedy the reduced coupling of the Y QD transition to the H-polarized cavity mode by increasing the laser power, while the emitted single photons are efficiently collected by the V-polarized cavity mode. This also means that the Y QD transition is well suited to be used as a single-photon source if it is resonantly excited, and, since the X transition can be neglected due to sufficient QD fine-structure splitting, it resembles a nearly perfect two-level system.

Here we investigate the dependency between maximum single-photon rate and single-

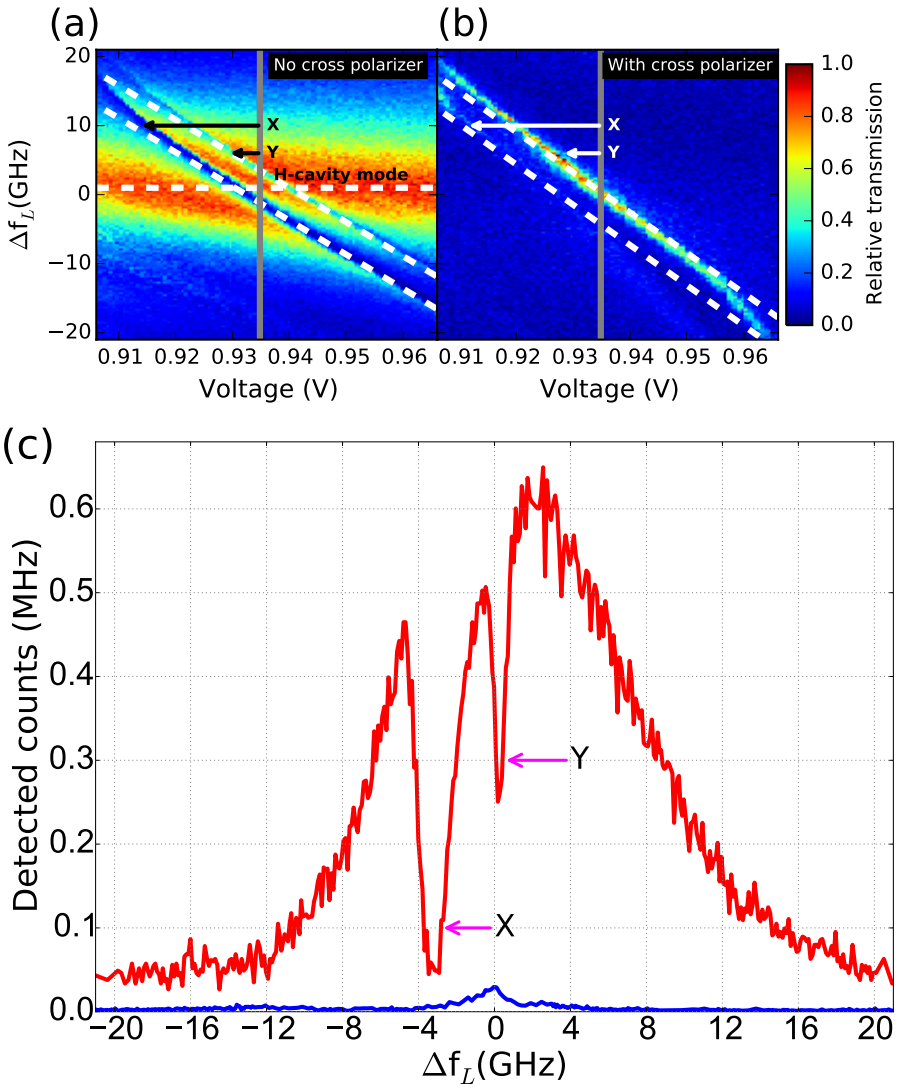

Figure 7.5: (a, b) False color plots of resonant transmission as a function of laser frequency and gate voltage. In (a), the incident laser light is polarized along the H cavity axis, and the transmitted light is detected without polarization selection. In (b), the remnant laser light is filtered out using a crossed polarizer oriented along the V-polarized cavity mode, to select the photons coherently scattered from the Y-transition of the QD. Panel (c) shows cross sectional plots (red line: without polarization selection, blue line: with crossed polarizer, scan time 1 s) at a gate voltage of 0.935 V, indicated by the grey line in (a) and (b). The X and Y QD transitions and the H-polarized cavity mode are labeled.

photon purity that is achievable with the present device. For this, we first perform continuous-wave resonant spectroscopy experiments with a single-frequency diode laser.

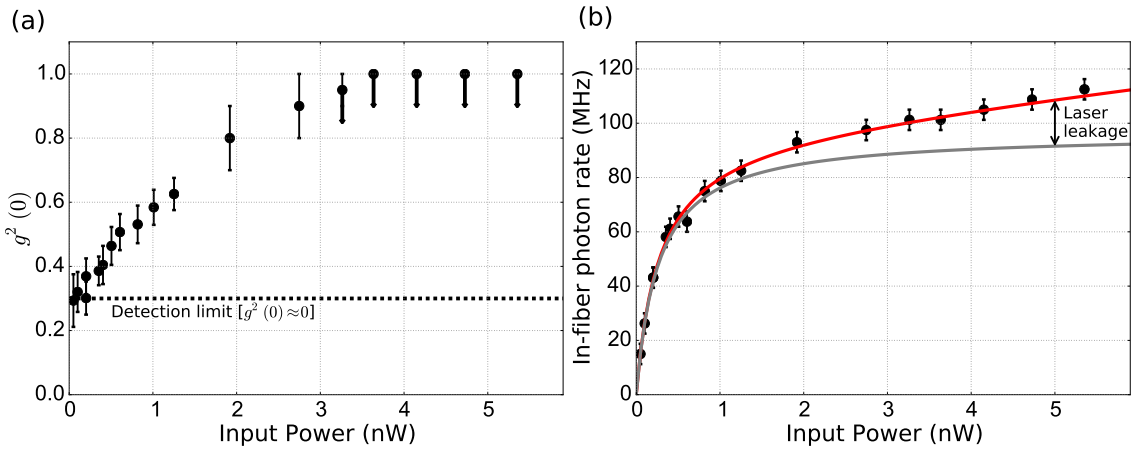

Figure 7.6: Measurement of the second-order correlation function $g^{(2)}(0)$ versus the incident laser power under continuous-wave excitation (a). The dashed line indicates the approximate limit on $g^{(2)}$ set by the detector jitter (two-detector instrument response function full width $\approx 532\,\mathrm{ps}$, see section 7.9.2 for details). (b) Simultaneously measured single-photon rate (corrected for detection efficiency). The fit (red line) takes into account the saturation of the QD transition (grey line), as well as residual laser light due to non-perfect polarization extinction.

We measure the second-order correlation $g^{(2)}(\Delta\tau = 0)$ and the flux of emitted photons as a function of the incident laser power (Fig. 7.6(a, b)). In the correlation measurements, we observe a lower limit of $g^{(2)}(0) \approx 0.3$, which is due to limited timing accuracy due to detector jitter; this is confirmed by comparing to reference measurements using short laser pulses (see section 7.9.2). Further, we observe an increase in $g^{(2)}(0)$ with increasing laser power. Two-photon emission from a single quantum system should in principle be absent if it is excited with laser pulses much shorter than its lifetime. We suspect imperfect laser extinction, which should also be visible in the detected photon count rate, shown in Fig. 7.6(b): instead of a simple saturation behavior of the count rate as a function of input laser power P, we observe an additional linear background. We find that the photon rate can very well be fitted (red line) by $96.0\,\mathrm{MHz}/(1 + 0.26\,\mathrm{nW}/P) + 3.39\,\mathrm{MHz} \cdot \mathrm{nW}^{-1} \times P$, where the first part describes standard two-level system saturation [23] and is plotted separately with the grey line in Fig. 7.6(b), and the saturation power agrees well to previous results on similar devices [130]. The power-linear term is most likely due to imperfect polarization extinction of the exciting laser light. These measurements show that good single-photon performance is expected for an input power well below a nanowatt.

7.5 Second-order correlation measurements

For quantum photonic applications, single photons are required on-demand with precise timing. We realize this using a resonant (around 932.58 nm) pulsed laser with 20 ps pulse length and 12.5 ns period. These values are well-matched to the QD transition in the cavity as shown in Fig. 7.5(c). Using a pulsed laser, we are no longer limited by the jitter of the single-photon detectors and can obtain a more accurate value for $g^{(2)}(0)$. At a sufficient low power of 100 pW, we measure a second-order correlation of $g^{(2)}(0) = 0.037 \pm 0.012$ as shown in Fig. 7.7(a). Note that we did not use spectral filtering of the cavity emitted light, in contrast to previous investigations [2]. As we have investigated above, $g^{(2)}(0)$ is in our case most likely limited by imperfect extinction of the excitation laser light.

7.6 Indistinguishability measurements

Next we determine the indistinguishability of two successively produced single photons. In order to create two excitation-laser pulses with exactly the same delay of 5.2 ns, we use a non-interferometric Michelson-type setup with adjustable delay. First, we examine the ideal case without losses and with ideal single-photon pulses (unity single-photon purity). We assume an excitation laser pulse spacing of 5.2 ns. We need to consider two double pulses and we label the photons as shown in Fig. 7.8(a): photon A at 0 ns, B at 5.2 ns, A' at 12.5 ns, and photon B' at 17.2 ns.

The detection is done using an unbalanced Mach-Zehnder interferometer, where one arm introduces a delay equal to the pulse delay (5.2 ns). Photon correlations behind the last fibersplitter are measured. We list all possible combinations of photons for which a two-photon detection event can happen with a particular temporal delay between the photons. In table 7.1 below, the first row indicates the delay between all possible photon combinations before the Mach-Zehnder interferometer. The lower 4 rows show the four possible pathways which pairs of photons can take, the number gives their relative delay at the single-photon detectors. The number of occurrences of a particular delay time is directly proportional to the detection probability. For example, it is 2 times more likely to detect two photons with $\Delta\tau$ =5.2 ns than it is with 2.1 ns, which agrees very well with the experimental data in Fig. 7.7(b).

	AA' (ns)	BB' (ns)	BA' (ns)	AB (ns)
Laser pulse delay (before detection in MZ)	12.5	12.5	7.3	5.2
first photon long arm	7.3	7.3	2.1	0
both photons short arm	12.5	12.5	7.3	5.2
both photons long arm	12.5	12.5	7.3	5.2
first photon short arm	17.2	17.2	12.5	10.4

Table 7.1: Table of arrival time differences $\Delta\tau$ of two-photon detection events.

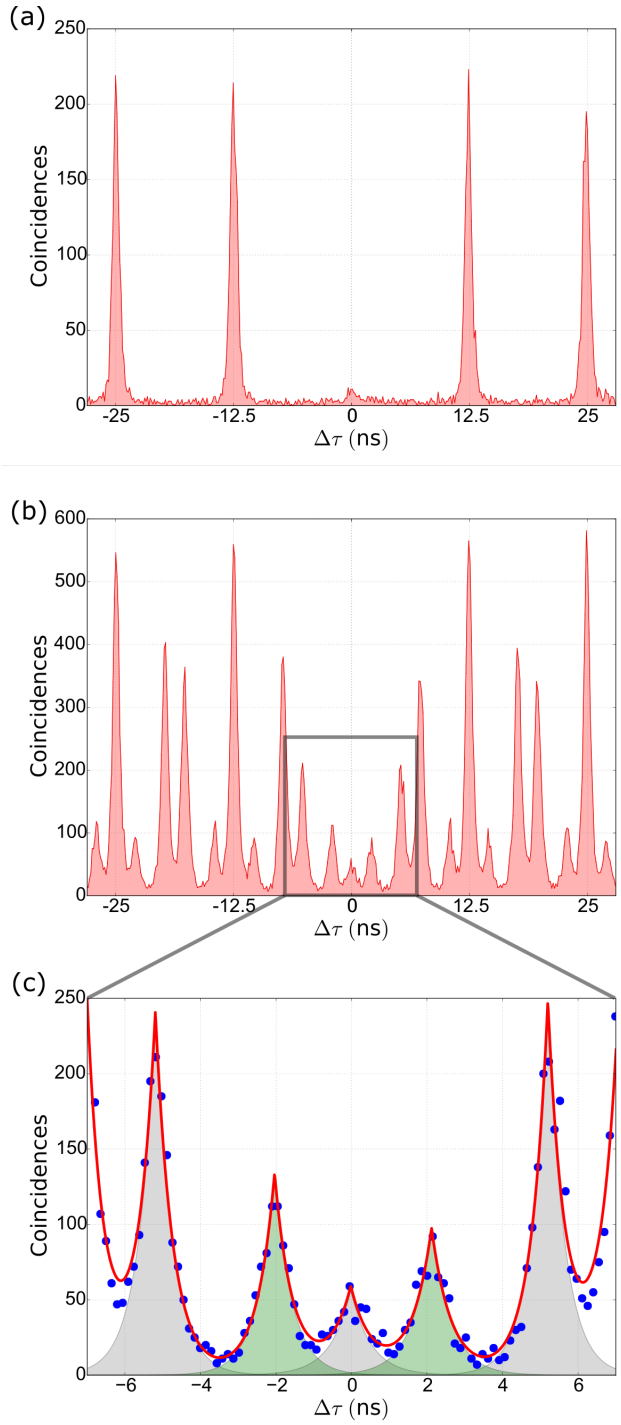

Figure 7.7: Photon correlations of the QD transition under pulsed excitation. (a): second-order correlation measurement, where $g^{(2)}(0) = 0.037$ is obtained from the integrated photon counts in the zero time delay peak divided by the average of the adjacent four peaks. (b): Photon-indistinguishability measurement for consecutive photons 5.2 ns apart. A magnified view around $\Delta\tau = 0$ and a double exponential fit of this data is shown in (c). Taking into account $g^{(2)}(0) = 0.037$ we obtain a measured indistinguishability of $M = 0.90$. Measurement time: 600 s (a), 1200 s (b, c).

If two consecutively produced single photons are indistinguishable, they will undergo quantum interference and "bunch", i.e. two-photon coincidences at $\tau = 0$ are expected to be absent in the ideal case. Due to this the "AB" event with $\Delta\tau = 0$ in table 7.1 disappears (see Fig. 7.7(c)).

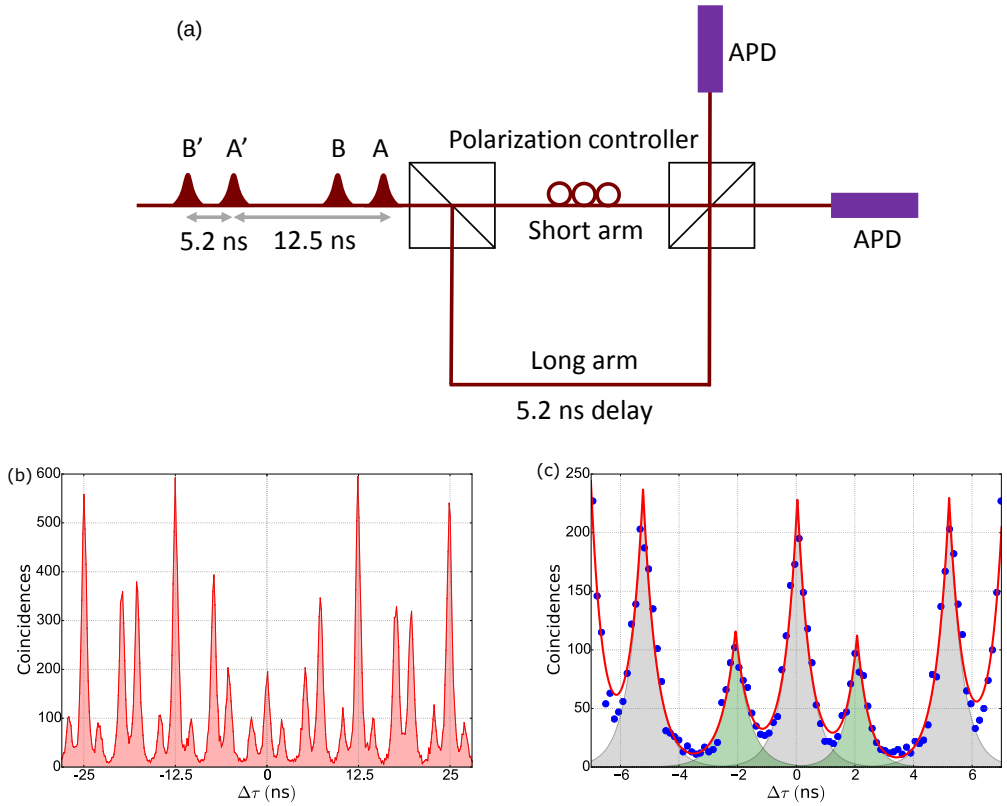

Figure 7.8: (a) Detection scheme for measuring the indistinguishability of consecutive photons. To compare to the case of distinguishable photons, we rotate the polarization in one arm of the interferometer. (b) The result for distinguishable photons is shown in (b, c), where photon bunching is suppressed and two-photon coincidences at $\Delta\tau = 0$ appear.

To contrast the indistinguishability measurement shown in Fig. 7.7(c) to the case where the photons are perfectly distinguishable, we perform an experiment where the photons are made artificially different by giving them orthogonal polarization. The result in Fig. 7.8(b) clearly shows the absence of Hong-Ou-Mandel type photon bunching by the strong correlations at $\Delta\tau = 0$. Fig. 7.8(c) shows a zoom-in with double-exponential fits to the measured data. This agrees excellently with the expectation in table 7.1, note that the $\Delta\tau = 0$ probability should be multiplied by two due to the coincidence of $\pm\Delta\tau$.

This model can be improved by taking into account the losses of the fibersplitters (we assume that both fibersplitters are identical) and a finite purity of the single-photon pulses. To do this, we follow the procedure of Ref. [9]: The probability for a detection event at the center peak normalized by the repetition rate and detection efficiency is given by

$$A_{CP} = (R^3T + TR^3)(1 + 2g^{(2)}(0)) - 2(1-\varepsilon)^2 MT^2R^2, \tag{7.2}$$

where M is the mean wave function overlap or indistinguishability, $(1-\varepsilon)$ is the visibility of the Mach-Zehnder interferometer and R and T are the reflection and transmission coefficients of the fibersplitters. Comparing this to the probability for a detection event at $\Delta\tau = \pm 5.2$ ns, we obtain

$$M = \frac{1}{(1-\varepsilon)^2}\frac{R^2+T^2}{2RT}\left[(1 + 2g^{(2)}(0)) - \frac{A_{CP}}{A_{-5.2ns} + A_{5.2ns}}(2 + 2g^{(2)}(0))\right]. \tag{7.3}$$

We independently measured for our fibersplitters the following values for the reflectivity, transmittivity and visibility: $R = 0.469$, $T = 0.531$, $(1-\varepsilon) = 0.96 \pm 0.1$. From double exponential fits in Fig. 7.7(c) we determine the coincidence probability ratio to be $\frac{A_{CP}}{A_{-5.2ns}+A_{5.2ns}} = 0.12 \pm 0.004$. Combined with the single-photon purity measurement with $g^{(2)}(0) = 0.037 \pm 0.012$ (Fig. 7.7(a)), we obtain for the indistinguishability $M = 0.90 \pm 0.05$. If the correction due to the finite $g^{(2)}(0)$ is removed and we only correct for the beamsplitters in the detection scheme we obtain a bare indistinguishability value of $M = 0.83 \pm 0.05$. The deviation from $M = 1$ might be due to residual spectral diffusion or nuclear-spin induced dephasing mechanisms.

7.7 Brightness measurements

Finally, to determine the brightness of the device, i.e. the fraction of laser pulses that produces a single photon in the detection fiber, we carefully characterize our setup including optical loss and detector efficiencies.

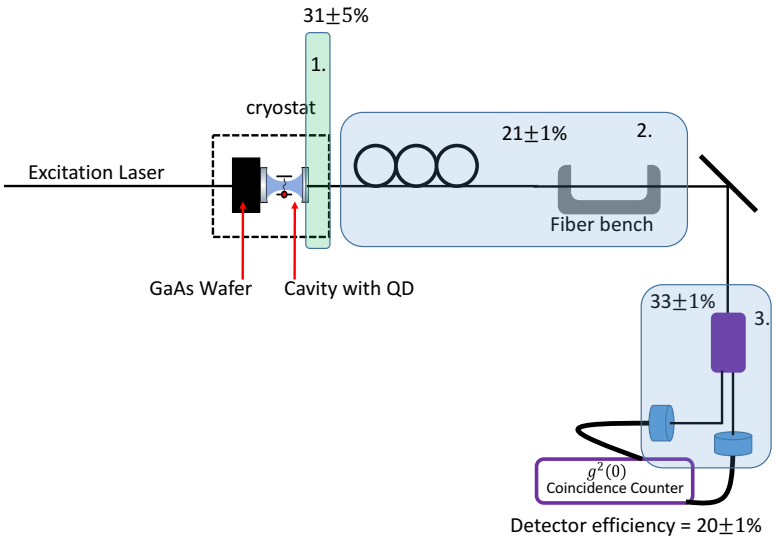

Figure 7.9: Characterization of the transmission in the detection part of the setup.

In order to determine the in-fiber brightness, we have to determine the transmission from the collection fiber to our detectors, and the detection efficiency. Fig. 7.9 show the relevant parts:

1. Fiber splice in the cryostat with $T = 31 \pm 5\%$. This is determined by measuring the off-resonance cavity mirror reflection through the fiber, where we assume that the cavity mirror reflectivity is close to unity and that there are no losses between mirror and fiber tip, which is supported by the absence of any interference signal (assumed uncertainty 5 %).

2. The polarization setup transmission is reduced by the free-space polarizer, the fiber bench, and the fiber mating sleeves, resulting in $T = 21 \pm 1\%$, which has been measured directly.

3. The single-photon detection setup with a detector efficiency of 20 ± 1 % and multimode fibersplitter with $T = 33 \pm 1\%$.

This results in a total detection efficiency of 0.43 ± 0.08 %; equivalently, therefore, our measured single-photon detection rate of 17 kHz corresponds to 4.0 MHz in the fiber directly after the sample, or an in-fiber brightness of 0.05 ± 0.01. The reduced value

is due to an imperfect spectral alignment of the QD and cavity mode, while the fiber coupling efficiency is excellent at 85%, or 94% of its optimum.

7.8 Conclusion

In conclusion, we have shown a prototype of a fully fiber-coupled solid-state single-photon source that produces on-demand single photons with a purity of 0.96 ± 0.01, indistinguishability of 0.90 ± 0.05 and a brightness of 0.05 ± 0.01, with fiber-coupling efficiency of 0.85 ± 0.11. These figures are already promising for exploring small optical fiber-based quantum networks such as for boson sampling. From another point of view, we have demonstrated a first all-fiber integrated cavity-QED based photonic quantum gate that filters out single photons from pulses of coherent laser light. A next step is charging of the QD with a single electron or hole spin to create a quantum memory [131] which makes the device usable as a quantum node for remote entanglement generation, quantum key distribution, and distributed quantum computation.

7.9 Supplemental material

7.9.1 System Parameters

In order to theoretically model the QD cavity-QED system we use an extended version of a model for a two-level system in an optical cavity driven by a classical coherent laser field. Using QuTiP [37, 38] we solve numerically the quantum master equation in the rotating wave approximation. Details about the model we use to fit the data can be found in Ref. [5].

We iteratively fit the simulation results to experimental data (shown in Fig. 7.10). We obtain a cavity splitting of $f_{cavsplit} = 18 \pm 0.5$ GHz and a cavity decay rate $\kappa = 70 \pm 3$ ns^{-1}. Now we keep these parameters fixed and optimize the model for the case when only the H-polarized cavity mode is excited to obtain the remaining 4 parameters of our QD-cavity system (7.10). We find a QD-cavity coupling constant $g = 14 \pm 0.4$ ns^{-1}, a population relaxation rate of $\gamma^{||} = 1.0 \pm 0.4$ ns^{-1}, a pure dephasing rate of $\gamma^* = 0.4 \pm 0.3$ ns^{-1}, a QD fine-structure splitting of $f_{QDsplit} = 3.9 \pm 0.05$ GHz, and for the angle between the H-polarized cavity mode and the X QD transition $\phi = 17° \pm 2°$. The frequencies of the two fine-structure-split QD transitions in Fig. 7.10 are $f_{QDX} = -3.6$ GHz and $f_{QDY} = 0.3$ GHz, and the (relative) frequencies of the polarization split fundamental cavity modes are $f_{CavH} = 2.0$ GHz and $f_{CavV} = 20.0$ GHz.

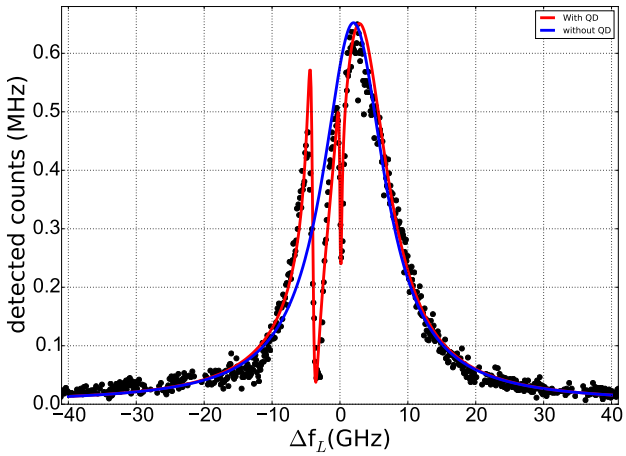

Figure 7.10: Resonant transmission data of the two fine-structure split QD transitions in a polarization non-degenerate cavity. Black dots: experimental data, red line: theoretical model, blue line: empty cavity.

From these parameters we find a cooperativity of $C = \frac{g^2}{\kappa(\gamma^{||}/2+\gamma^*)} \approx 2.8$ which corresponds to a Purcell enhancement of the excited state decay rate of $F_p = \frac{4g^2}{\kappa\gamma^{||}} \approx 11.2$, assuming that the QD transition is on resonance with the cavity transition.

7.9.2 Detector response

Our second-order correlation function $g^{(2)}(\tau)$ measurements using two single-photon counters (SPCM-AQR-14) is limited by the timing jitter in the detectors and electronic equipment. In order to quantify this effect, we first determine the intensity auto-correlation function of 2 ps long light pulses, shown in Fig. 7.11(a). We obtain a FWHM of 532 ps.

Now we predict how this effects a continuous-wave measurement of the resonance fluorescence 2nd-order correlation function (Fig. 7.6), which requires knowledge of the relaxation rates that determine the $g^{(2)}(\tau)$ dip width. Therefore we calculate the expected $g^{(2)}(\tau)$ by solving the quantum master equation, which is shown as the black curve in Fig. 7.11(b). Now we can convolute this with the detector response that was determined in Fig. 7.11(a), and we obtain the purple curve. We see that this agrees very well with the measured $g^{(2)}(\tau)$ (red dots) and therefore we conclude that the continuous-wave measurement of $g^{(2)}(\tau)$ is largely limited by detector jitter.

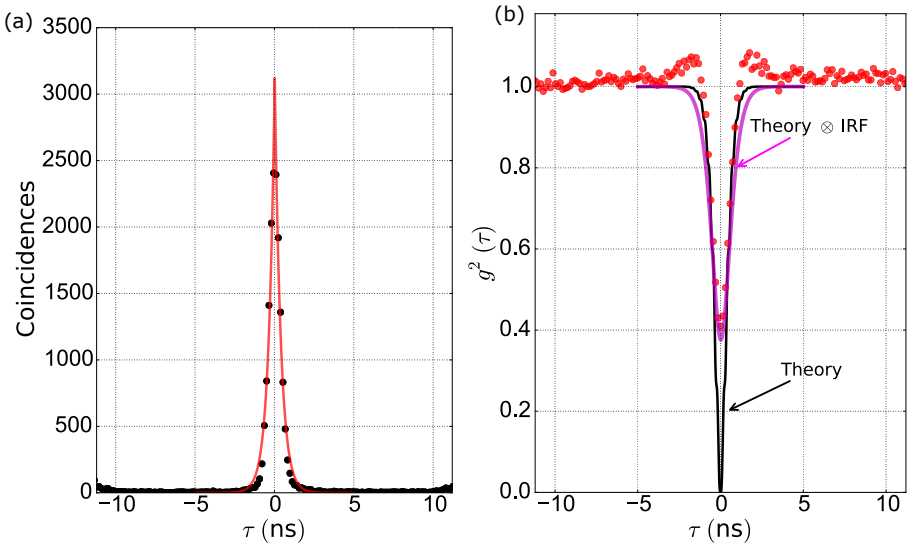

Figure 7.11: (a) The two-detector response to a 2 ps light pulse is well fitted by a double-exponential function. (b) Comparison of the experimental data with the convolution (purple curve) of the detector response with the theoretical prediction (black curve).

7.9.3 Cavity mode to fiber coupling efficiency

- The cavity out-coupling constant η_{cav} is determined from free-space measured on-resonance cavity reflectivity via $R = (1 - \eta_{cav})^2$, from which we obtain $\eta_{cav} = 0.2 \pm 0.02$. Based on the mirror design we would expect $\eta_{cav} = \frac{2\kappa_m}{\kappa} \approx \frac{28}{70} \approx 0.4$, our reduced value suggests that optical scattering and/or absorption is present.

- The fiber-coupling efficiency η_{out} is then obtained from the on-resonance reflectivity measurement through the fiber (Fig. 7.12) where we obtain $R = 0.68 \pm 0.02$, and with $R = (1 - \eta_{cav}\eta_{out})^2$, this results in $\eta_{out} = 0.85 \pm 0.11$.

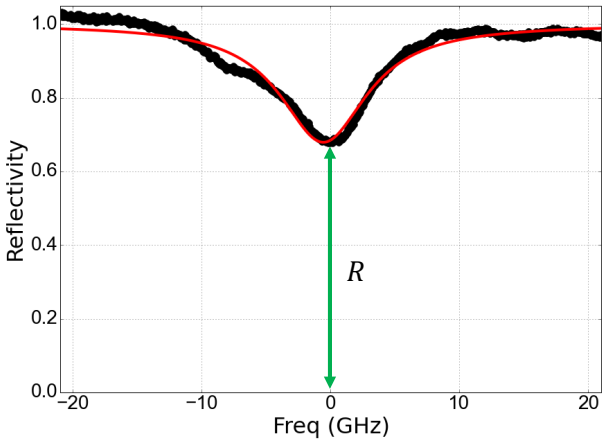

Figure 7.12: Through-fiber reflection measurement for determination of fiber coupling efficiency.